Rotor performance and turbulent wake simulations of a scaled helicopter rotor in hover using wall-modeled large-eddy simulations

By Z.T. Stratton,† S.T. Bose‡ AND J. Svorcan¶

A scaled helicopter rotor in hover is studied using wall-modeled large-eddy simulations (WMLES). Performance is evaluated for three thrust conditions at varying grid resolutions and validated with experimental measurements. Capturing the effects of the laminar-turbulent transition over the blade, and the subsequent impact on blade forces, poses a significant challenge for the equilibrium wall model. Results indicate that a mesh with around two grid points in the turbulent boundary layer predicts forces that indicate fully turbulent flow over the blade. Meshes with around seven grid points in the turbulent boundary layer can capture some transitional impact on blade forces, despite not accurately predicting transition location. Further confirmation of viscous force impact on rotor loads was evaluated with simulations using a blowing-suction trip to force transition and a wall-model sensor to act as a crude transition model.

1. Introduction

The accurate prediction of rotorcraft flow fields remains a challenging problem for computational fluid dynamics (CFD). This is especially true under hover conditions, where the blades are rotating at high RPM through quiescent air, resulting in length and timescales that vary by orders of magnitude. This encourages simulations to implement approximations and simplifications to keep computational costs low. However, steady-state approaches, such as Reynolds-averaged Navier-Stokes (RANS), show an average error of 2.4% when compared with measured values of figure of merit (FM) (Yamauchi & Young 2009). The FM, a measure of the rotor efficiency, is very sensitive to the predicted rotor torque and thrust. Rotorcraft design requires the ability to accurately predict the FM within 0.5% in order to estimate payload capacity (Chaderjian & Ahmad 2015). Early attempts to reduce this error in RANS focused on resolving the wing-tip vortices that are shed from the rotor-blade tips and the subsequent interaction with the passing blade. Accurately predicting the initial strength and trajectory of these vortices, along with the subsequent blade-vortex interaction (BVI), using adaptive mesh refinement, significantly improved rotor load predictions at high thrust conditions (Chaderjian 2012). However, at low thrust, RANS predicted excessive turbulent eddy viscosity in the rotor wake during the BVI that resulted in an underprediction of FM. Chaderjian & Buning (2011) showed that detached-eddy simulation (DES) could provide an appropriate length scale to the near-wall RANS model that resolves the issue related to excessive turbulent eddy viscosity and improves FM predictions at low thrust. State-of-the-art rotor flow computations continue to utilize DES; however, recent challenges include finding a RANS

† US Navy, Naval Air Warfare Center Aircraft Division, U.S. Navy
‡ Cascade Technologies, Inc.
¶ University of Belgrade, Serbia

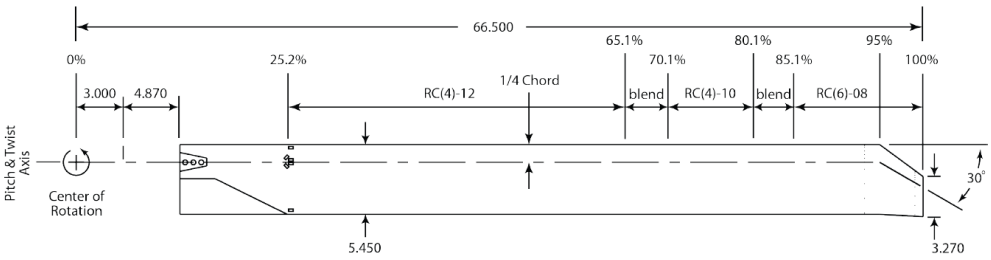

FIGURE 1. PSP blade planform.

formulation in the near-wall region that can sufficiently predict the laminar-turbulent transition in the boundary layer that can occur for rotors operating in certain Reynolds number regimes (Jain 2022).

It is desirable to not have to rely on choosing the best formulation of the RANS model in order to predict accurate rotor loads. While wall-resolved LES can provide significant improvements in accuracy over RANS in such cases, resolving the viscous sub-layer can still be prohibitively expensive for complex geometries at high Reynolds numbers, such as a rotor blade (Choi & Moin 2012). However, WMLES approaches significantly reduce near-wall grid requirements by modeling the influence of the inner-layer eddies (Bose & Park 2018). The capability of WMLES to predict rotor loads and FM for a rotor in hover is currently unknown, especially for blades that exhibit boundary layer transition.

The objective of this study is to examine the predictive capability of WMLES when applied to the pressure-sensitive paint (PSP) rotor in hover. The PSP rotor is an advanced helicopter blade designed by the U.S. Army and NASA to be used as an open-source experimental test case for CFD validation. This rotor-only WMLES simulation will utilize a moving mesh approach to determine rotor loads and FM and to assess the wall models ability to capture transition effects. The grid requirements and computational cost will also be discussed.

2. Problem description

This CFD study is based on the four-blade PSP rotor, which was tested in the Rotor Test Cell at NASA Langley Research Center (Overmeyer & Martin 2017). The rotor planform is shown in Figure 1. It is a scaled rotor based on U.S. Government RC-series airfoils, with a linear twist of $-14°$, radius of 66.5 in, and chord length of 5.45 in. The blade operates at a Re of 1.05×10^6, based on tip velocity and tip chord length; additional blade properties are shown in Table 1. While the blade can flex under load, aeroelastic effects will not be considered. Instead, predefined coning angles will be applied to the model, as described in Table 2; this is an upward angle, out of the rotation plane, and will be applied at the hinge located at 3.0 in from the hub center (Jain 2022). Three collective angles—6°, 8°, and 10°—will be studied; the collective is the blade angle with respect to the pitch and twist axis with higher collectives corresponding to higher rotor thrust. In the test, this rotor is mounted on the ROBIN-Mod7 fuselage; however, in this study it will be applied as an isolated rotor in hover. The test collected force measurements where the flow transitioned from laminar to turbulent naturally as well as measurements when the transition was forced using small raised dots along the leading edge at $x/c = 0.05$.

Rotor radius	66.5 in.
Solidity (σ)	0.1033
Tip chord	3.27 in.
Reference chord	5.45 in.
RPM	1150
Collective pitch angle	6°–12°
Tip Mach number	0.58
Tip Reynolds number	1.05×10^6

TABLE 1. PSP blade properties.

Collective	Cone
6°	−0.680°
8°	0.085°
10°	0.900°

TABLE 2. PSP coning angles.

3. Formulation and computational setup

3.1. *Flow solver and turbulence models*

The CharLES LES code, developed by Cascade Technologies, is used to solve the compressible, time-dependent, filtered Navier-Stokes equations for this isolated rotor in hover configuration. CharLES utilizes a density-based finite-volume method on unstructured grids, where fluxes are computed with a second-order scheme (Ham 2006). The time integration uses an explicit third-order Runge-Kutta scheme. The mesh generation is handled by Stitch, a tool within the CharLES suite, which is automatic and based on the computation of Voronoi diagrams (Bres 2017). This method results in a smooth mesh of nearly isotropic cells throughout the domain, which is well suited for LES. CharLES has implemented a moving mesh solver, in which a portion of the mesh can move within a stationary mesh. At the interface between the moving and stationary meshes, the Voronoi diagrams are rebuilt, such that the mesh remains continuous, without the need for interpolation. This implementation is utilized for this rotor in hover problem.

CharLES has implemented a wall-stress-based wall model that significantly reduces the near-wall grid requirements, which is used throughout this study. This model's equations are based on the algebraic formulation of the one-dimensional equilibrium stress model (Kawai & Larsson 2010). These equations are solved at each wall-adjacent cell centroid at each time step for wall shear stress, which serves as the Neumann boundary conditions for the momentum equations. This wall model does not account for unsteadiness or pressure gradient effects in the inner layer solution. To account for the sub-grid-scale stresses, the static model by Vreman (2004) is used.

3.2. *Computational domain and simulation details*

The computational domain used for this study is shown in Figure 2. It consists of a cylindrical moving domain within a cylindrical stationary far-field domain. At the interface, cells are matched one to one without overlap. The rotor is simulated in free air, so facility effects are not considered. A total pressure boundary condition is applied to the top and sides of the far-field domain with an outlet pressure boundary condition on the far-field surface below the rotor. The rotor-blade surfaces are set as adiabatic walls, and the algebraic equilibrium wall model is specified for these surfaces. The flow is initialized

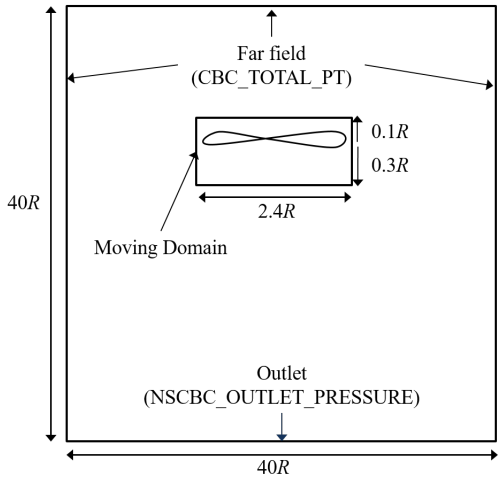

FIGURE 2. Computational domain with relevant scales. Characteristic boundary conditions (CBC) are applied to the far-field and outlet regions.

to zero velocity, pressures and temperatures are set to match the test conditions, and the rotor is started impulsively at the target RPM. Three separated collective angles of 6°, 8°, and 10° were examined.

In order to validate the force measurements for the forced transition case, a blowing-suction trip was implemented in CharLES. The blowing and suction were set via a sinusoidal signal with a specified amplitude and frequency. This is applied as a boundary condition to a strip on the bottom and top of the blade, located at $0.05c_{ref}$ with a width of $0.05c_{ref}$. To further understand the impact of transition on the force measurements, a rudimentary wall-model sensor was implemented, which specifies a laminar or turbulent form of the wall shear stress depending on an Re based on viscous length and velocity scales and a sub-grid-scale viscosity.

The grids used in this study are summarized in Table 3. The M0 grid is used only to initialize the flow field over 15 rotor revolutions; the finer meshes are then interpolated on this solution and run for a further two to five rotor revolutions to collect force data. Grids M0 through M2 are based on isotropic Voronoi meshes, whereas the M3 mesh uses a strand-based grid generation that allows for anisotropic refinement near the walls. The quantity δ_{turb}/Δ gives the approximate number of grid points in the turbulent boundary layer measured at the mid-chord at the rotor tip, where δ_{turb} is the turbulent boundary layer thickness based on a flat-plate approximation and Δ is the average grid spacing in the boundary layer. The M3 mesh also adds a ring of refinement around the blade tips to better capture the blade-tip vortex and BVI with a spacing of $0.05c_{tip}$. The background mesh in the moving domain is set to $0.1c_{tip}$ on all grids. Figure 3 shows the grid structure for M3 near the blade tip, with details of the leading and trailing edges showing the strand growth in the boundary layer.

All simulations are run using a Courant-Friedrichs-Lewy number of 3.5, which corresponds to 0.006 degrees per time step and 0.0009 degrees per time step for M1 and M3, respectively. This corresponds to approximately 3900 CPU-hours per revolution and 92000 CPU-hours per revolution for M1 and M3, respectively. The simulations are run on the U.S. Department of Defense Warhawk and Narwhal clusters using GPU resources. Using 40 GPUs, the M3 grid computes one rotor revolution in 48 hours.

	Wall normal	y^+_{avg}	δ_{turb}/Δ	Total cell count	CPU-hour/rev
M0	$0.025c_{tip}$	450	$\sim$	29M	$\sim$
M1	$0.00624c_{tip}$	110	2	58M	4000
M2	$0.00312c_{tip}$	55	4	300M	25000
M3 (strand)	$0.000781c_{tip}$	11	7	250M	92000

TABLE 3. Mesh details.

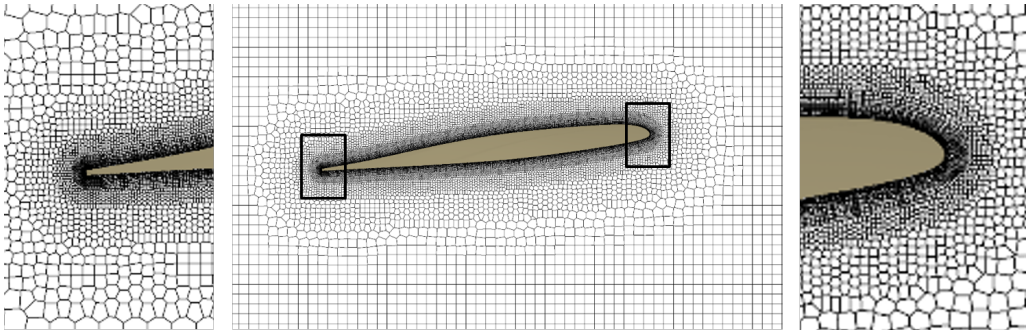

FIGURE 3. M3 grid structure based on Voronoi diagrams, with strand elements near the walls. Image taken at the rotor tip, within the $0.05c_{tip}$ refinement region.

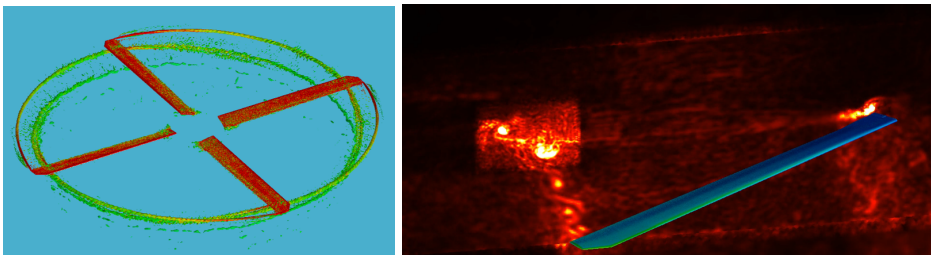

(a) (b)

FIGURE 4. Rotor in hover at 8° collective. (a): Iso-surfaces of Q-criterion. (b): Vorticity magnitude; yellow indicates regions of high vorticity.

4. Results

Figure 4a shows the iso-surfaces of Q-criterion for an 8° collective on the finest mesh, and Figure 4b shows a contour plot of vorticity magnitude. This figure shows that the tip vortices are well resolved for around 180° of wake age, before the mesh begins to coarsen significantly. The contour shows how the added resolution in the blade-tip region helps to maintain strong vorticity in the tip vortex. The BVI is also well resolved, where a smaller secondary vortex that forms as a result of this interaction can be seen in the Q-criterion iso-surface.

The main force quantities of interest for a rotor in hover are the torque coefficient (C_Q), thrust coefficient (C_T), and FM. The FM is the main performance parameter for a rotor in hover, and it represents the ratio of the ideal power to actual power. The closer this parameter is to one, the more efficient the rotor is; this is used during the design process to estimate how much payload can be carried. These parameters are defined as

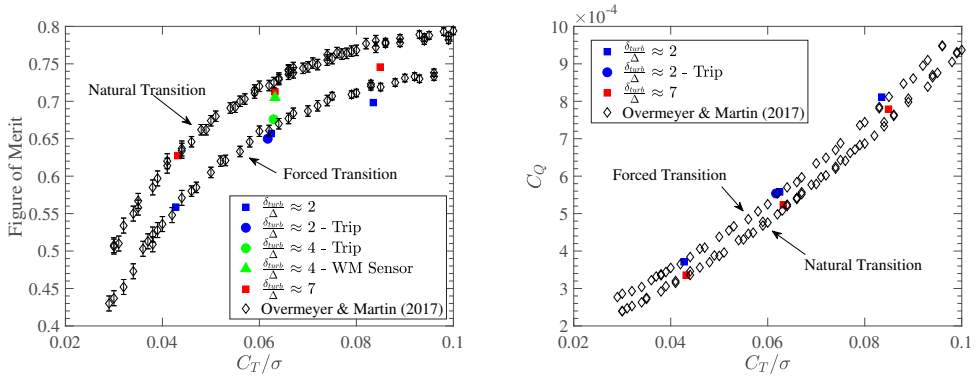

(a) (b)

FIGURE 5. (a): Figure of merit as a function of thrust. (b): Torque coefficient as a function of thrust. Two sets of experimental data by Overmeyer & Martin (2017) are included: one curve where the blades exhibit natural transition and another curve where transition is forced on both the top and bottom surfaces.

$$C_Q = \frac{Q}{\rho(\Omega R)^2 RA}, \tag{4.1}$$

$$C_T = \frac{T}{\rho(\Omega R)^2 A}, \tag{4.2}$$

$$FM = \frac{C_T^{3/2}}{\sqrt{2}C_Q}, \tag{4.3}$$

where Q is the rotor torque, T is the rotor thrust, Ω is the rotor rotational speed, R is the rotor radius, A is the rotor disk area, and ρ is the free-stream density.

Figure 5a shows the FM plotted as a function of thrust, and the computed results are compared with the test data by Overmeyer & Martin (2017). The test data include the FM where the flow transitioned from laminar to turbulent flow naturally over the blade as well as data that forced the flow to transition using trips on the leading edge of both the top and bottom of the blades. For the CFD data, the different colors indicate different mesh sizes, and different shapes indicate different handling for the rotor-blade wall boundary condition. In general, the WMLES correctly captures the trends in FM over a range of thrusts. At high thrusts, flexible blades tend to exhibit more significant unwinding of twist; therefore, the rigid-blade assumption results in an underprediction of FM at high thrust.

The squares in Figure 5 indicate that there is a large difference in computed force when the mesh is refined, with the coarse mesh predicting forces that are more in line with the forced transition measurements. This may indicate that with so few grid points in the boundary layer, the wall model is overpredicting wall shear stress, resulting in what would indicate fully turbulent flow over the rotor blades and thus falling close to the experimental measurements for forced transition. When the grid is refined, the FM approaches the experimental values for natural transition, indicating lower predicted shear stresses, despite not accurately resolving transition; this will be discussed later. The

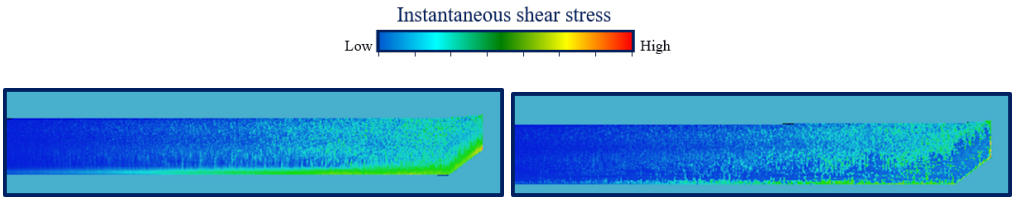

(a) (b)

FIGURE 6. Instantaneous wall shear stress contours for (a) the tripped case and (b) the wall-model sensor case on M2.

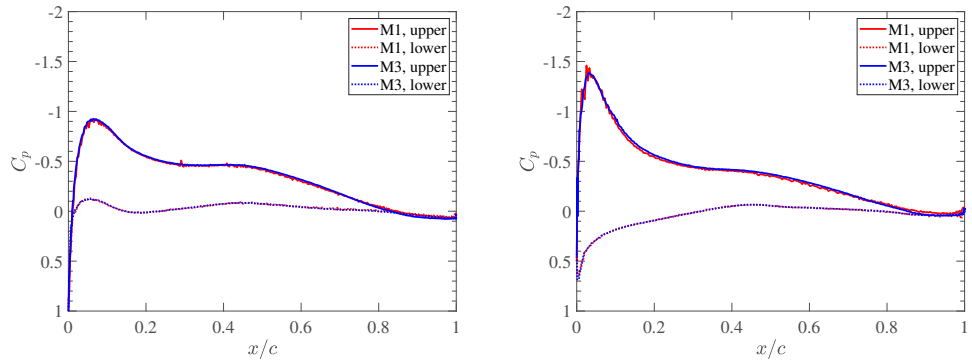

(a) (b)

FIGURE 7. Pressure coefficient for M1 and M3 at 8° collective. (a): $r/R = 0.825$. (b): $r/R = 0.973$.

torque coefficient, plotted in Figure 5b, shows that the consequence of natural transition (i.e., decrease in viscous forces) is to reduce torque and increase thrust.

To get a better understanding of how the predicted forces are influenced by the wall shear stress, a blowing and suction boundary condition was implemented to trip the flow and ensure that the boundary layer was fully turbulent over the entirety of the blade; these data are shown as circles in Figure 5. With only two grid points in the boundary layer, the tripped case shows a similar FM as the untripped case. With four points in the tripped boundary layer, the FM increases, but is still within the experimental uncertainty for the forced transition measurements. If a wall model sensor is applied at this resolution instead of a trip, shown as a triangle, the FM increases by around 0.03, approaching the natural transition measurements. This sensor is acting as a crude transition model by increasing the portion of the blade that sees a laminar wall shear stress. Figure 6 compares the instantaneous wall shear stress between the tripped and sensor cases, showing smaller values of wall shear stress over the leading portion of the blade.

The discrepancy between the coarse and fine meshes in Figure 5 appears to be related to the viscous stresses. To rule out pressure-related discrepancies, the pressure coefficient is plotted in Figure 7 for the coarse and fine meshes at two locations. The figure shows very similar pressures, indicating that inviscid effects are well resolved by the WMLES even on the coarse mesh, and that solution differences are indeed confined to the near-wall region.

To further understand wall shear stresses and transition, between the two grid reso-

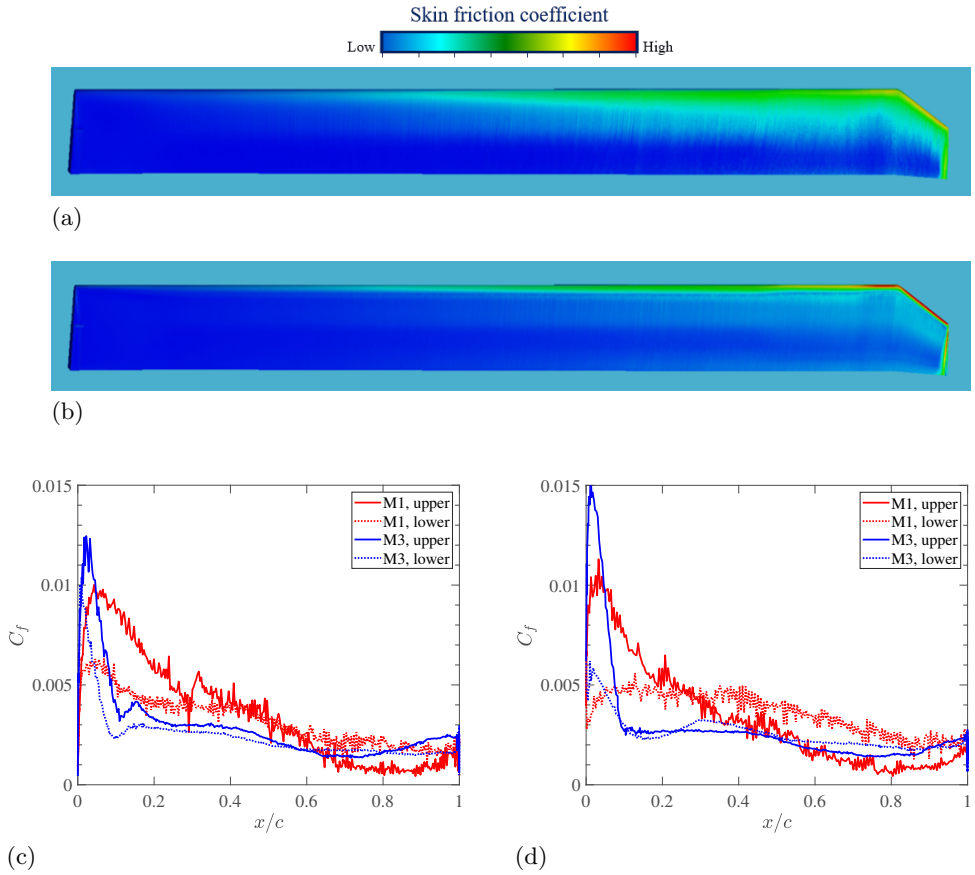

FIGURE 8. (a,b): Time-averaged skin friction coefficient for M1 (a) and M3 (b) meshes. (c,d): Slices of time-averaged skin friction coefficient at $r/R = 0.825$ (c) and $r/R = 0.973$ (d) for M1 and M3 meshes.

lutions, skin friction contours of the suction side and line plots are shown in Figure 8. The finer mesh shows a lower skin friction over a wider region of the blade compared with the coarse mesh. The line plots indicate that for the fine mesh, skin friction rapidly decreases around the leading edge, before increasing slightly and then decreasing again; this would suggest that the boundary layer transitions around an x/c of 0.2 at an r/R of 0.825. On the other hand, no such transition is seen in the coarser mesh; instead, a smaller peak and higher sustained skin friction are seen over the blade.

To assess the accuracy of the predicted transition seen in the finer mesh ($\delta_{turb}/\Delta = 7$), the skin friction is compared directly with experimental measurements of transition at 8° and 10° collective angles in Figure 9. In general, the boundary layer on the suction side should transition earlier as the collective angle (i.e., thrust) increases. The WMLES results can capture this trend; however, the location of the transition is incorrect for the 8° collective case. On the pressure side, the boundary layer is not expected to transition until an x/c of 0.9; however, the computed transition is much closer to the leading edge.

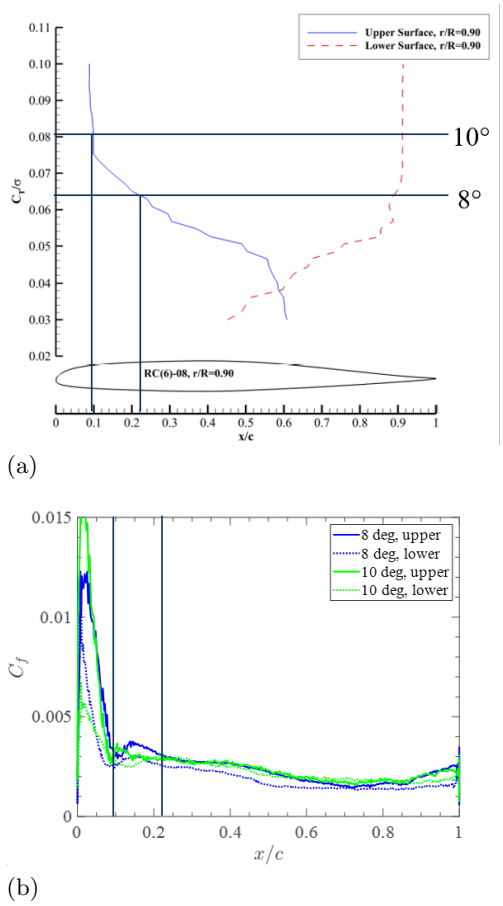

FIGURE 9. Experimentally measured transition locations on the upper and lower blade surface at $r/R = 0.9$, from Overmeyer & Martin (2017) (a), are compared to predicted transition locations based on skin friction coefficient from WMLES (b). Horizontal lines mark the C_T/σ that corresponds to 8 and 10 degree collective angles and vertical lines mark where transition was measured on the upper surface for those collective angles and where it is expected to occur in the WMLES.

5. Conclusions

WMLES was used to simulate an isolated rotor in hover for three collective angles and predicted FM within around 2% at low and medium thrust and within 4% at higher thrust. However, there is some uncertainty in the predictions because blade flexing, facility effects, and downwash effects were not considered. Despite these assumptions, WMLES shows promise for the rotor in hover problem, with the ability to capture BVIs and inviscid forces. Capturing viscous forces remains a challenge; however, with as few as seven grid points in the boundary layer, the equilibrium wall model was able to capture some transition effects. Tripping the flow showed good agreement with the forced transition measurements. A wall model sensor that acted as a crude transition model also showed some potential for rotors that exhibit free transition.

The computational cost of simulating a rotor in hover using WMLES is reasonable on modern high-performance computers when a fully turbulent boundary layer is expected. The finest mesh considered in this study, 250M cells, required two days of simulation

time on 40 GPUs to complete one rotor revolution. At this grid resolution, the laminar instabilities that trigger transition are not accurately resolved. If these instabilities were to be resolved, the cost would increase exponentially.

Acknowledgments

The authors acknowledge the computational resources provided by the Department of Defense (DoD) High Performance Computing Modernization Program, specifically the DoD Air Force Research Laboratory and Navy DoD Supercomputing Resource Center systems. Support by Dr. John Spyropoulos at the Naval Air Warfare Center Aircraft Division and Dr. Steve Martens at the Office of Naval Research is gratefully acknowledged.

REFERENCES

Bose, S. T. & Park, G. I. 2018 Wall-modeled large-eddy simulation for complex turbulent flows. *Annu. Rev. Fluid Mech.* **50**, 535–561.

Bres, G. A., Bose, S. T., Emory, M., Ham, F. E., Schmidt, O. T., Rigas, G. & Colonius, T. 2018 Large-eddy simulations of co-annular turbulent jet using a Voronoi-based mesh generation framework. *AIAA Paper* 2018-3302.

Chaderjian, N. M. 2012 Advances in rotor performance and turbulent wake simulation using DES and adaptive mesh refinement. *Seventh International Conference on Computational Fluid Dynamics*, pp. 1–25.

Chaderjian, N. M. & Ahmad, J. U. 2015 Navier-Stokes assessment of test facility effects on hover performance. *Proceedings of the American Helicopter Society 71st Annual Forum*, pp. 658–681.

Chaderjian, N. M. & Buning, P. G. 2011 High resolution Navier-Stokes simulation of rotor wakes. *Proceedings of the American Helicopter Society 71st Annual Forum*, pp. 375–392.

Choi, H. & Moin, P. 2012 Grid-point requirements for large-eddy simulation: Chapman's estimates revisited. *Phys. Fluids* **24**, 011702.

Ham, F., Mattsson, K. & Iaccarino, G. 2006 Accurate and stable finite volume operators for unstructured flow solvers. *Annual Research Briefs*, Center for Turbulence Research, Stanford University, pp. 243–261.

Jain, R. 2022 CFD hover performance and transition predictions on the PSP and HVAB rotors using CREATE-AV Helios. *AIAA Paper* 2022-1549.

Kawai, S. & Larsson, J. 2010 Wall-modeling in large-eddy simulation: length scales, grid resolution, and accuracy. *Annual Research Briefs*, Center for Turbulence Research, Stanford University, pp. 39–46.

Overmeyer, A. D. & Martin, P. B. 2017 Measured boundary layer transition and rotor hover performance at model scale. *AIAA Paper* 2017-1872.

Vreman, A. W. 2004 An eddy-viscosity subgrid-scale model for turbulent shear flow: algebraic theory and applications. *Phys. Fluids* **16**, 3670–3681.

Yamauchi, G. K. & Young, L. A. 2009 A status of NASA rotorcraft research. Tech. Publ. 2009-215369, NASA.